ADVANCED FUNCTIONAL MATERIALS
www.afm-journal.de

Structure-Induced Stability in Sinuous Black Silicon for Enhanced Hydrogen Evolution Reaction Performance

*Margaret Patrick, Fan Yang, Waltteri Vakki, Jeffery A. Aguiar, and Jing Gu**

Clean energy infrastructures of the future depend on efficient, low-cost, long-lasting systems for the conversion and storage of solar energy. This is currently limited by the durability and economic viability of today's solar energy systems. These limitations arise from a variety of technical challenges; primarily, a need remains for the development of stable solar absorber–catalyst interfaces and improved understanding of their mechanisms. Although thin film oxides formed via atomic layer deposition have been widely employed between the solar absorber–catalyst interfaces to improve the stability of photoelectrochemical devices, few stabilization strategies have focused on improving the intrinsic durability of the semiconductor. Here, a sinuous black silicon photocathode (s-bSi) with intrinsically improved stability owing to the twisted nanostructure is demonstrated. Unlike columnar black silicon with rapidly decaying photocurrent density, s-bSi shows profound stability in strong acid, neutral, and harsh alkaline conditions during a 24-h electrolysis. Furthermore, scanning transmission electron microscopy studies prior to and post electrolysis demonstrate limited silicon oxide growth inside the walls of s-bSi. To the authors' knowledge, this is the first time structure-induced stability has been reported for enhancing the stability of a photoelectrode/catalyst interface for solar energy conversion.

1. Introduction

In accordance with our growing global energy demands, engineering of clean energy conversion systems has become increasingly important. Of the many approaches currently being researched, incident solar light remains the largest untapped fuel source with roughly 100 000 TW of solar energy striking the earth annually.[1] With a current annual energy consumption of ≈19 TW and a projected use of 42 TW at the end of the century, solar energy alone is sufficient to power all energy needs for the foreseeable future, therefore efficiently absorbing and converting the incident solar spectrum is paramount to a sustainable clean energy cycle.[1,2] To date, solar energy has been used to drive many processes including electrosynthesis, nitrogen fixation, carbon capture, and the reduction of water or carbon dioxide.[3–7] While each process has its own importance, efficient solar-driven reduction of water to hydrogen (H_2) is highly desirable for general energy production due to the abundance of raw materials and low environmental impact. Achieving solar H_2 production from water would alleviate the need for consumable materials such as oil while producing only water in the process, which can be reused to complete a clean energy cycle limited only by the absorption of sunlight and lifetime of the system.

While many approaches have been taken to reach new heights in solar energy conversion, optimizing the semiconducting material remains the primary challenge facing advancement of the field. Semiconductors are responsible for the conversion of incident light into excitons which can be separated into holes (h^+) and electrons (e^-), resulting in the generation of an electronic potential capable of driving many electrochemical reactions including the reduction of water to H_2 or carbon dioxide to methanol.[6] While some methods aim to optimize light harvesting and conversion by utilizing III–V semiconductors and/or complex multijunction interfaces, these systems are limited by cost, stability, and unmatched band positions at each junction, making it difficult to commercialize or achieve water splitting without applying an external bias.[8–11] In light of this, silicon (Si) is increasingly being chosen as the photoabsorber in photoelectrochemical (PEC) systems as it is a low-cost earth-abundant semiconductor with a small band gap (E_g = 1.12 eV) suitable for the absorption of the solar spectrum with band edge potentials appropriate for the reduction of water to H_2.[12] Recently, focus has shifted toward nanostructured or nanoporous Si materials due to their superior light absorption properties and highly tunable morphologies.[13–15] These materials, commonly termed "black silicon" due to their extremely low reflectivity and matte black appearance, can be fabricated using many methods including metal-assisted chemical etching (MACE), electrochemical etching, reactive ion etching, and laser treatment.[16] While each technique has its own merits,

M. Patrick, Prof. F. Yang, W. Vakki, Prof. J. Gu
Department of Chemistry and Biochemistry
San Diego State University
5500 Campanile Drive, San Diego, CA 92182-1030, USA
E-mail: jgu@sdsu.edu
Dr. J. A. Aguiar
Idaho National Laboratory
Nuclear Materials Department
2525 Fremont Avenue, Idaho Falls, ID 83415, USA
Dr. J. A. Aguiar
Lockheed Martin
Advanced Technology Center
3251 Hanover Street, Palo Alto, CA 94304, USA
The ORCID identification number(s) for the author(s) of this article can be found under https://doi.org/10.1002/adfm.202008888.

DOI: 10.1002/adfm.202008888

MACE is of particular interest as it is a facile process requiring no specialized equipment which can be tuned to produce an enormous array of morphologies.[16,17]

Although typical columnar nanoporous black silicon (c-bSi) produced by the MACE method has higher activity and lower reflectivity than planar Si, it is prone to rapid degradation resulting in a continuous severe loss of current density; electrolysis performed using c-bSi without a catalyst or protection scheme has only been shown to be stable for 300 s in strong acid.[12] In order to combat these stability issues, few viable protection methods have been developed. The vast majority passivate the surface by depositing conductive optically transparent thin films using atomic layer deposition (ALD). This technique is advantageous due to conformal coverage, precise thickness control, and low defect density.[18] Single layers of aluminum oxide (Al_2O_3) or titanium dioxide (TiO_2) deposited between the semiconductor and catalyst have been shown to improve stability. One study by Choi et al. showed stability for 12 h in a strong acidic environment after applying a 2.3 nm-Al_2O_3 passivation layer onto c-bSi with Pt catalyst, while another noted that a TiO_2 layer ≈20 nm-thick is required to passivate the surface of Si nanowire composites and potentially other porous substrates due to cracking or pinhole formation.[19,20] A similar study on GaAs found a 26 nm-layer of TiO_2 could sustain 80% current density after 60 h in neutral conditions using Pt as a catalyst for PEC water splitting.[21] Unfortunately, this is still not sufficient for practical applications. Several studies have attempted to surpass this limit using dual-layer schemes, including one focused on protecting the semiconductor–catalyst interface as well as the semiconductor itself.[22] In this study, a 20 nm-layer of TiO_2 was deposited onto c-bSi before depositing the catalyst. A second 2 nm-TiO_2 layer was deposited atop the catalyst to protect the semiconductor–catalyst interface, resulting in stability for 110 h. While these results are promising, ALD is an expensive technique which has not been realized for large-scale use, thus, there remains a need to stabilize the bSi surface without requiring an additional protective layer.

Recently, our group discovered a sinuous nanoporous bSi interface (s-bSi) (**Figure 1**c,d), which maintained prolonged performance under strong acidic conditions (>24 h) in an unbiased microbial PEC hydrogen evolution reaction (HER) system.[23] In this work, we demonstrated the stability of bSi can be improved without any protection schemes by modifying the sub-interface morphology. To our knowledge, this is the first time structure-induced stability has been reported for enhancing stability on a photoelectrode/catalyst interface for solar energy conversion. However, the stablization mechanism of this interface is still unexplored. Herein, by the direct comparsion with the common linear nanostructure of c-bSi, the enhanced stability of s-bSi is attributed to the impairment of oxygen diffusion through the twisted s-bSi channels thereby reducing the rate of SiO_x growth on the interface. Thus, the oxygen-deficient environment of the sinuous

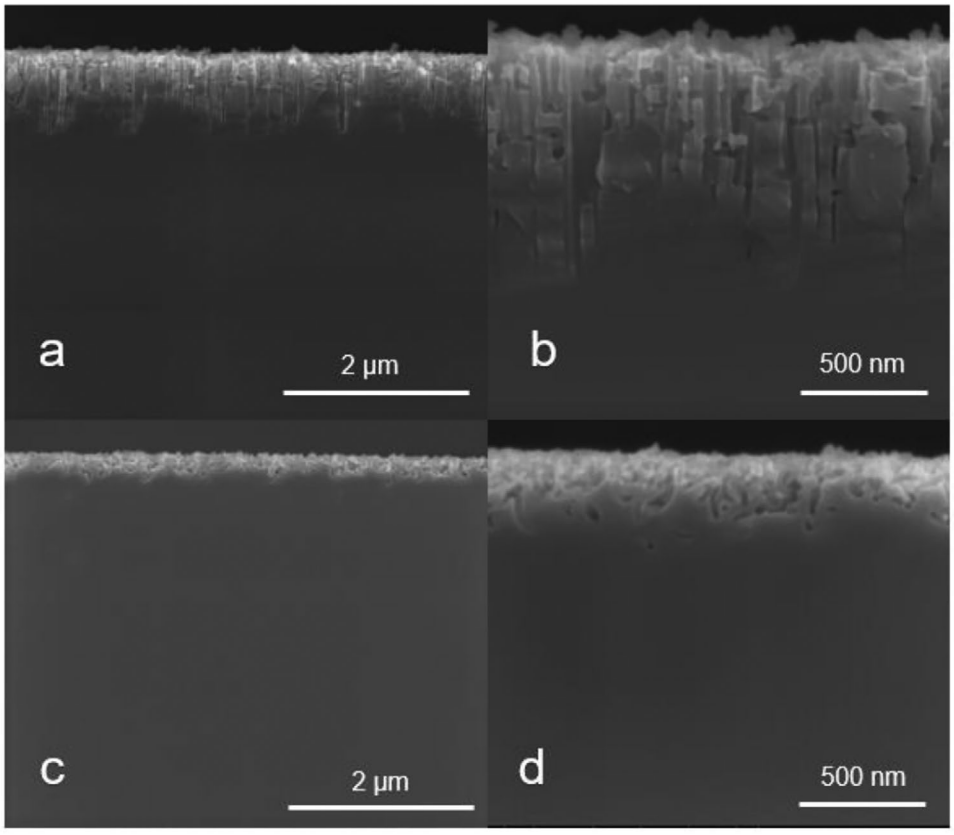

Figure 1. SEM characterization. Cross-sectional SEM images of a,b) c-bSi and c,d) s-bSi. Linear channels can be seen in c-bSi, while s-bSi exhibits twisted sinuous channels. Both samples were produced using MACE, where s-bSi was prepared using IPA as an additive in the etching solution.

structure maintains the chemical integrity of the bSi interface and significantly improves stability.

2. Morphologies and Formation Mechanism

When viewed from the surface, the structures of s-bSi and c-bSi are nearly indistinguishable (Figure S1, Supporting Information), however, cross-sectional SEM reveals extremely different subsurface morphologies. As seen in Figure 1, the subsurface interface of s-bSi is randomly twisted with a pore depth of ≈300 nm while c-bSi has straight nanopores perpendicular to the surface with a depth of ≈600 nm. The pore width in both s-bSi and c-bSi is ≈30–50 nm. Both samples are produced by the MACE method, a wet chemical process which employs a noble metal catalyst deposited on the surface of Si to reduce hydrogen peroxide (H_2O_2) in the "burial" etching solution (**Scheme 1**a). The hole generated in this process is injected into the Si substrate causing the oxidation of Si to form SiO_x, which reacts with hydrofluoric acid (HF) in the burial solution to form H_2SiF_6 and H_2 gas.[16] Due to the accumulation of holes at the metal/Si interface, SiO_x will continuously form underneath the metal particles and react more rapidly with HF than areas of exposed substrate. Straight columnar channels perpendicular to the surface are typically produced; this is the case with c-bSi.

To produce s-bSi, the same technique is applied with the addition of isopropanol (IPA) to the burial solution. The IPA induces changes to the channel morphology, causing the formation of twisted channels rather than columnar. Adding IPA as a surfactant in potassium hydroxide (KOH) burial solutions has been previously shown to produce pyramid-shaped bSi, where IPA facilitates the release of H_2 while slowing the etching rate.[24–26] In another study on Si nanowire (NW) fabrication, a higher concentration of IPA was reported to generate a slow etching rate thereby reducing the length of the NWs. In this process, IPA was suggested to act as a modulation reagent which reduces the number of etchant molecules present at the Si surface.[27] In our case, we hypothesize that the IPA acts similarly to a modulation reagent at the metal/Si interface during the etching process, unevenly passivating holes from reacting with HF, leading to nonuniform Si oxidation and thus undirected channel formation (Scheme 1b). This is observed in s-bSi with directionally non-preferential etching relative to the strictly perpendicular etching in c-bSi. Burial solutions containing other organic solvents such as acetone and toluene were also tested; similar sinuous channels were formed, indicating these solvents can functionalize similarly to create s-bSi (Figure S2, Supporting Information). In this work, we investigate the differences between s-bSi and c-bSi in terms of stability, electrochemical activity, charge transfer, reaction kinetics, and elemental analysis to determine the origins of enhanced HER performance in s-bSi.

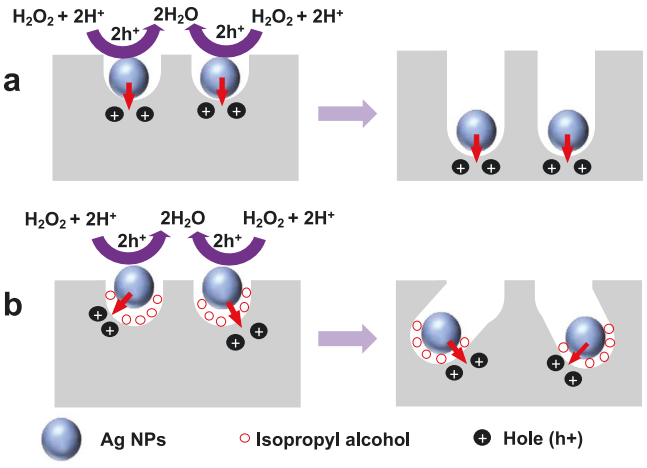

Scheme 1. MACE mechanism. Illustrations of a) a typical MACE process for synthesizing c-bSi where blue dots indicate metal catalyst and black dots indicate holes and b) the MACE process for synthesizing s-bSi with the addition of isopropyl alcohol (IPA) (red circles). The red arrows indicate etching direction.

3. Stability under Various pH Conditions

To focus on effects resulting from differences in bSi morphology, platinum (Pt) was used as the hydrogen evolution catalyst for all experiments in this study as it is a model HER catalyst with well-defined properties.[28,29] Both samples followed identical Pt deposition procedures for control. Initially, linear sweep voltammetry (LSV) was performed in 0.5 M H_2SO_4 (pH 0.9), 0.5 M Na_2SO_4 (pH 8.2), and 1.0 M KOH (pH 13.9) to determine the difference in onset and saturation potentials in a range of pH conditions (Figure S3, Supporting Information). Originally, pH 7 phosphate buffer was used for testing in neutral conditions; however the resulting current densities exceeded 70 mA cm^{-2} for both the tortuous and columnar morphologies. These high values are likely due to side reactions between the buffer and the sample, therefore Na_2SO_4 was used to achieve a near-neutral pH without side reactions. The onset and saturation potentials were found to be similar for both samples prior to electrolysis. The onset potentials established by LSV were determined to be 0.229 and 0.248 V versus RHE in 0.5 M H_2SO_4 for s-bSi and c-bSi, respectively. A large negative shift (≈400 mV) in these values was observed for both samples in neutral conditions relative to acidic electrolyte while little difference (<200 mV) was observed between basic and neutral conditions (Table S1a, Supporting Information). In all pH conditions, post-24 h electrolysis LSVs of s-bSi showed a slight decrease in saturation and onset potentials relative to the prior-electrolysis LSVs (Table S1b, Supporting Information). Comparatively, in neutral and basic conditions, the onset and saturation potentials of c-bSi shifted significantly more negative after 24 h, in agreement with the stability tests. In acidic conditions, the onset potential of c-bSi does not change much, however it's limiting current density does decrease significantly which indicates degradation of c-bSi.

The above results indicate the HER activities of s-bSi and c-bSi are similar and are not influenced by the subinterface morphology. Relative stability was then compared by performing electrolysis for 24 h in each electrolyte at the respective saturation potentials determined by LSV. The s-bSi photoelectrode outperformed c-bSi in all tested pH conditions

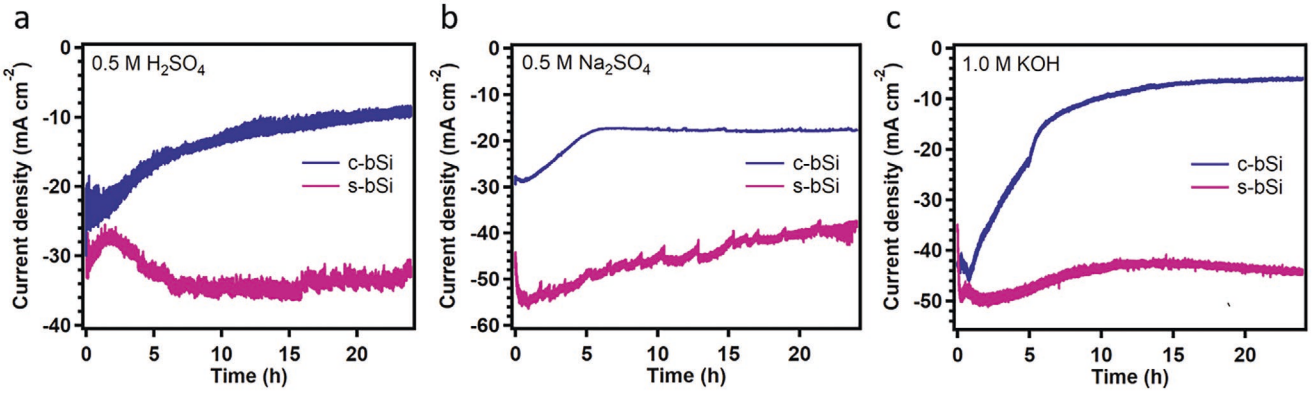

Figure 2. Stability comparison. Photocurrent density of c-bSi and s-bSi during 24-h electrolysis at respective saturation potentials under 1 sun irradiation in a) 0.5 M H_2SO_4 (pH 0.9), b) 0.5 M Na_2SO_4 (pH 8.2), and c) 1.0 M KOH (pH 13.9).

(**Figure 2**). While both suffered from current density losses, s-bSi maintained a much higher proportion of initial current density in all pH conditions. Under acidic and basic conditions, s-bSi maintained over 90% current density after 24 h while c-bSi only had 58% and 14% of its initial current density remaining, respectively. The tortuous morphology was also superior in neutral conditions with 81% current density remaining compared to 59% for c-bSi after 24 h. These results correlate well with the superior durability of s-bSi previously observed in the microbial PEC system.[23]

4. Photon-To-Current Conversion Efficiency

In order to understand the origins of enhanced stability in s-bSi, the PEC properties of both photoelectrodes were investigated by measuring the incident photon-to-current efficiencies (IPCE) between 400 and 1000 nm at the HER saturation potential where the contribution of the dark current is minimal (**Figure 3**a). For longer wavelengths (600–900 nm), both electrodes exhibited efficiencies around 70% before dropping sharply at 1000 nm. The 1000 nm efficiency drop can be attributed to

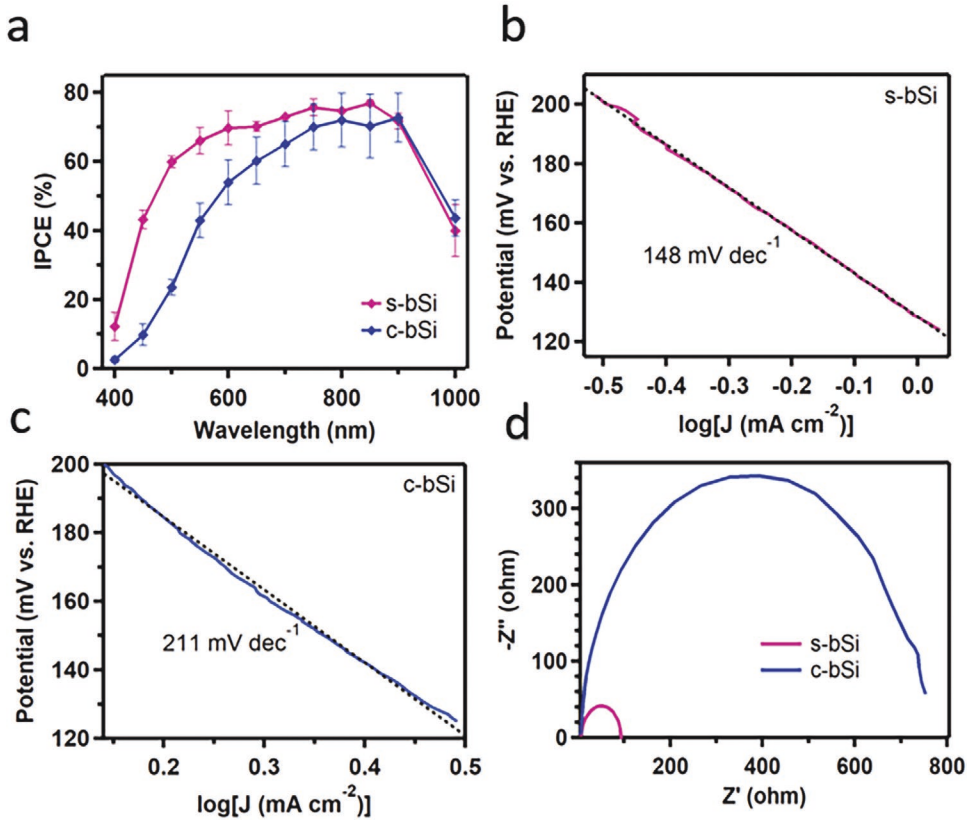

Figure 3. Electrochemical activity. a) IPCE of s-bSi and c-bSi measured at respective saturation potentials, b,c) Tafel plots of s-bSi and c-bSi, respectively, and d) Nyquist impedance plots measured at respective onset potentials (0.229 and 0.248 V vs RHE). All tests were performed with Pt catalyst in 0.5 M H_2SO_4 under 1 sun irradiation.

the bandgap of Si (1.12 eV), where the energy of photons after 1000 nm will not be able to excite electrons from the valance band to the conduction band.[30] At the shorter wavelengths, s-bSi vastly outperformed c-bSi with IPCE values almost five times higher at 400 nm before dramatically decreasing between 450 to 600 nm to reach near a unity ratio at 600 nm and beyond (Figure S4, Supporting Information). One study on a set of 400–700 nm Si NWs found that IPCE decreased with increasing NW length as shorter wavelength photons cannot reach the junction and achieve charge separation if the diffusion distance is too long. When this happens, carrier recombination occurs rather than conducting HER.[31] The difference in IPCE was found to be negligible at wavelengths greater than 700 nm, correlating well with this study.[31] Although the channel depth in the s-bSi and c-bSi is similar (≈300–600 nm), the channels of s-bSi are distributed mostly near the surface (≈300 nm) while channels of c-bSi penetrate deeper (≈600 nm). As a consequence of this difference, it is more difficult for photons to reach the Si surface in c-bSi as pore depth increases, thus potentially resulting in increased charge recombination. Wavelengths near 600 nm and longer will be absorbed by the bulk, thus similar IPCE should be observed for both compounds at longer wavelengths.[31]

$$\text{Volmer step}: H^+ + e^- \rightarrow H_{ad} \quad (1)$$

$$\text{Heyrovsky step}: H^+ + H_{ad} + e^- \rightarrow H_2 \quad (2)$$

$$\text{Tafel step}: 2H_{ad} \rightarrow H_2 \quad (3)$$

5. Impedance of the Semiconductor–Catalyst Junction

Further understanding of the differences in HER performance was elucidated by comparing the Tafel slopes for both samples to determine the reaction kinetics. Tafel slopes correlate directly with the dependence of the catalytic reaction rate on applied overpotentials. It is well known that the value of the Tafel slope can be used to distinguish the rate-determining step in HER. More specifically, a Volmer, Heyrovsky, or Tafel rate-determining step, as shown in Equations (1)–(3), would give slope values of 120, 40, and 30 mV dec^{-1}, respectively.[32,33] By comparison, the Tafel slope of Pt is 29–30 mV dec^{-1}. The Tafel slopes were calculated, using a program developed by Agbo et al., to be 148 and 211 mV dec^{-1} for s-bSi and c-bSi, respectively, corresponding well with the LSV results and indicating that both samples proceed via similar reaction kinetics (Figure 3b,c).[33,34] These slopes (>120 mV dec^{-1}) indicate the Volmer reaction is likely the rate-determining step, where the large values may be due to an unavoidable pre-existing SiO_x layer between photoelectrode and catalyst in both morphologies.

Electron transport kinetics were then compared using electrochemical impedance spectroscopy in acidic conditions at the respective onset potentials with Pt catalyst. Analysis of the Nyquist plots (Figure 3d) revealed a large difference in impedance, where the charge transfer resistance across the electrode–electrolyte interface, R_{ct}, was found to be 744.5 and 86.2 Ω for c-bSi and s-bSi, respectively, after fitting using the equivalent circuit model (Figure S5, Supporting Information). The comparable electrolyte solution resistance (R_s) for c-bSi (10.73 Ω) and s-bSi (6.903 Ω) was expected since both electrodes were tested in the same electrolyte. The smaller resistance at the s-bSi/Pt/electrolyte interface indicated by R_{ct} suggests superior charge transfer kinetics compared to c-bSi. Given that both samples were exposed to air for an equal amount of time and underwent identical treatment prior to testing, the difference in resistance must either arise from differences in effective catalyst loading or an inequal rate of surface degradation. In the latter case, deterioration of the nanoporous structure or the formation of silicon oxides (SiO_x) would lead to higher resistance at the electrode/electrolyte interface. If this degradation is more rapid for c-bSi, the expected R_{ct} values would be higher than for s-bSi. To ensure differences in catalyst loading were not the cause of the decreased impedance in s-bSi, the distribution of Pt on the surface of both samples was mapped using SEM coupled with energy dispersive X-ray spectroscopy (EDX) (Figure S6, Supporting Information). The spectra were very similar for both samples, showing uniform distribution of both large and small Pt clusters. Quantitative analysis revealed 3.80 and 4.33 wt% Pt for c-bSi and s-bSi, respectively, indicating catalyst loading was comparable. The corresponding particle size distributions of c-bSi and s-bSi were compared, where a slightly larger average size was found on s-bSi (≈42 nm) relative to c-bSi (≈34 nm) (Figure S7, Supporting Information). Since SEM characterization revealed almost indistinguishable surface structure, this analysis confirms that the differences in charge transfer and electrochemical activity do not result from the discrepancies in catalyst loading on the two bSi surfaces, and thus must arise from the twisted subsurface morphology.

6. Pre- and Post-Electrolysis Interface Comparison

Given that the electrochemical activity and electron transport kinetics are similar for both compounds while the impedance and stability are vastly different, it is likely that charge transfer on the nanostructured surface is more easily hindered in c-bSi than s-bSi. Since Si spontaneously reacts in the presence of oxygen to form SiO_x, we hypothesize that the linear channels of c-bSi are prone to faster surface oxidation, thus causing these photoelectrodes to degrade faster regardless of the pH of the environment. Oxides like SiO_2 are known to have very large band gaps (≈9.0 eV), thereby the formation of SiO_x can effectively prevent charge transfer between the photoelectrode and catalyst.[35] Furthermore, SiO_x is unstable under both acidic and alkaline conditions.[36] For example, SiO_x can react with sulfuric acid to produce silicon dioxide, sulfur dioxide and water, or react with sodium hydroxide to form silicate complexes. Thus, the formation of silicates and silicon dioxide could increase the corrosion rate of the photoelectrodes. To test this hypothesis, scanning transmission electron microscopy (STEM) coupled with EDX was performed on both samples prior to electrolysis to determine the oxygen content on the surface of the channel walls (**Figure 4**). Elemental carbon, oxygen, and silicon were clearly identified in the channels of both c-bSi and s-bSi. Elemental mapping shows a higher oxygen concentration

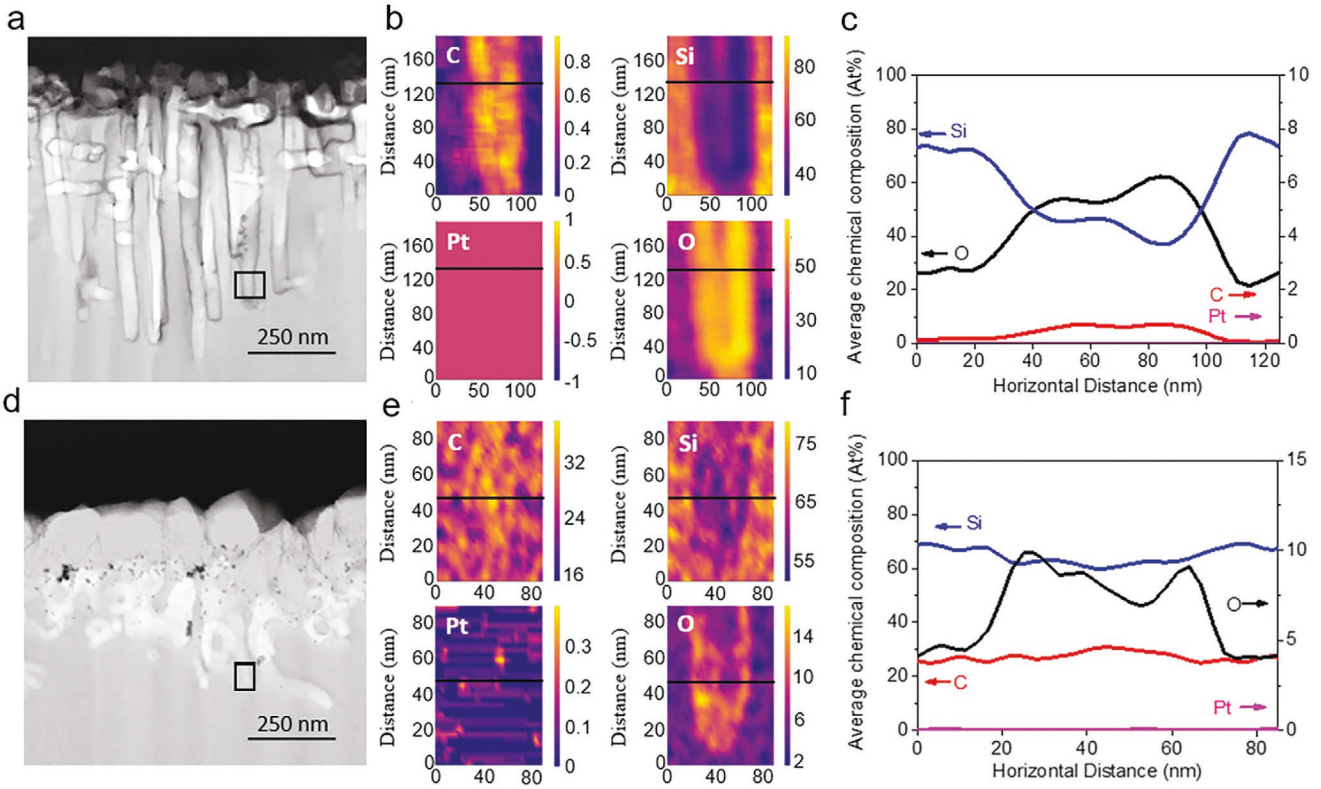

Figure 4. STEM and EDX. Cross-sectional STEM images of a) c-bSi and d) s-bSi prior to electrolysis. Elemental mapping of C, Si, Pt, and O on channel walls in b) c-bSi and e) s-bSi. c,f) Atomic composition line profiles taken across the channel diameters corresponding to black lines in (b) and (e), with O (black), Si (blue), Pt (pink), and C (red).

with brighter quantified elemental contrast on the walls of c-bSi compared to s-bSi. Atomic composition line profiles taken across the channel diameter confirmed this hypothesis, revealing a sixfold difference in oxygen atomic percentage between c-bSi (≈60%) and s-bSi (9%) prior to electrolysis (Figure 4c,g). No clear platinum signals were observed at the bottom of the channels where Pt content is negligible. These results suggest oxygen can diffuse more readily through the channels in c-bSi than s-bSi. Additional STEM and EDX analysis of s-bSi after 24-h electrolysis in acidic conditions revealed the oxygen content on the channel walls remains under 10% (Figure S8, Supporting Information). Moreover, the structure and morphology of the nanochannels in s-bSi are well preserved after 24-h electrolysis. This result correlates well with the electrochemical results, indicating s-bSi maintains its structural integrity by efficiently preventing the formation of SiO_x. Additionally, it is worth noting that the apparent decrease in overall oxygen concentration for s-bSi post-electrolysis can likely be attributed to the increase in carbon content after electrolysis that is possibly due to the decomposition of the epoxy used to seal the photoelectrodes.[37] In order to monitor the diffusion of oxygen in c-bSi during electrolysis in strong acidic solution, SiO_x growth was recorded at $t = 0$, 8, 16, and 24 h using cross-sectional SEM (**Figure 5**). After 8 h-electrolysis, large clusters of SiO_x can be seen forming on the channel walls at all depths. As the reaction progresses (16 h), more SiO_x forms at the interface. By 24 h, the channels of c-bSi are almost completely filled with SiO_x. In comparison, minimal amounts of SiO_x were observed in the channels of s-bSi as the reaction progresses (Figure S9, Supporting Information). This ex situ experiment indicates that oxygen can easily diffuse and induce the formation of SiO_x throughout the channels in c-bSi, while the twisted morphology of s-bSi likely hinders oxygen diffusion, thus slowing the oxidation process.

In addition to channel morphology, channel size likely influences the stability of bSi. In order to understand the influence of channel size on stability of a nanoporous Si photoelectrode, c-bSi with a larger pore size (≈200–250 nm) was synthesized (c_{LP}-bSi). STEM-EDX results demonstrate uniform distribution of Si, C, and O throughout the nanochannels with Pt mostly settled on top of the Si surface (Figure S10, Supporting Information). In contrast, c_{LP}-bSi showed poor stability during electrolysis under acidic conditions (0.5 M H_2SO_4), with an almost complete loss of photocurrent density after 10 h (Figure S11a, Supporting Information). Post-electrolysis cross-sectional SEM of c_{LP}-bSi correlates well with the electrolysis results, showing thorough destruction of the original nanostructure (Figure S11b, Supporting Information). The aforementioned results demonstrate that larger channel size in nanoporous bSi corresponds to easier oxidation and degradation under HER conditions.

7. Conclusion

The increased understanding of controlling semiconductor surface properties resulting from this study will greatly aid

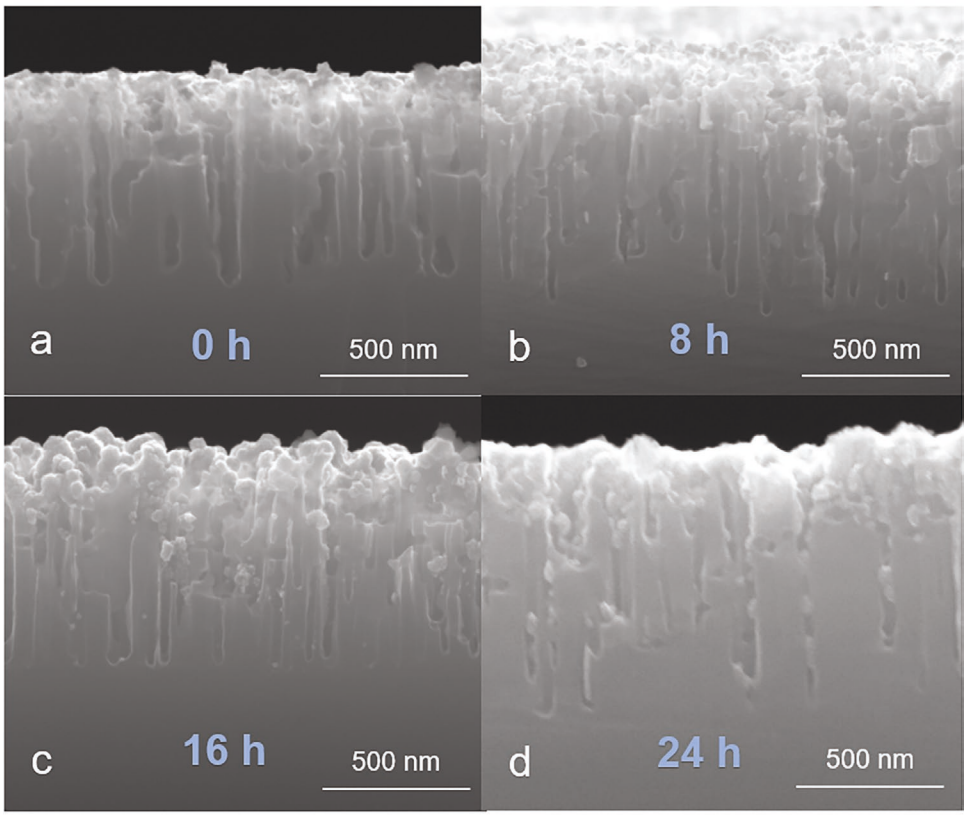

Figure 5. SiO_x growth on c-bSi. All samples were loaded with Pt were then used to perform HER for a) 0 h (control), b) 8 h, c) 16 h, and d) 24 h. SiO_x (light grey) growth is observed in contrast to the Si substrate (dark gray).

the future design and emerging applications of electronic devices, sensors, and photovoltaic protection schemes in addition to solar energy conversion. The differences in HER performance of columnar and sinuous nanoporous bSi were compared by measuring photocurrent density, PEC performance, charge transfer kinetics, and reaction kinetics. The PEC activity and electron transport kinetics were found to be similar for both photoelectrodes while the impedance and stability are vastly different. Since SiO_x forms spontaneously on Si in the presence of oxygen, surface oxidation would cause degradation of the system, loss of current density, and an increase in electrical impedance. We hypothesize that charge transfer on the nanostructured surface is more easily hindered in c-bSi than s-bSi due to more rapid oxidation of c-bSi. The twisted interface (s-bSi) demonstrated prolonged performance in acidic (0.5 M H_2SO_4), neutral (0.5 M Na_2SO_4), and alkaline (1.0 M KOH) conditions. This was further evidenced by detailed STEM-EDX analysis, where elemental mapping and atomic composition line profiles confirmed that six times more oxygen is found on the walls of c-bSi. Ex situ STEM and SEM analysis of post-electrolysis samples further demonstrated a near negligible increase in oxygen content in s-bSi after 24-h electrolysis in strong acid. In contrast, SiO_x can be seen forming quickly throughout the channels in c-bSi through cross-sectional SEM. These findings are the first report on the fundamental mechanisms for controlling subsurface morphology to induce prolonged photoelectrode stability as a viable alternative solution for stabilizing photocathode/catalyst interfaces.

8. Experimental Section

Columnar Nanoporous Black Silicon Fabrication: Small channel columnar bSi was prepared using a previously reported modification of the MACE method.[23] Briefly, the back side of a 525 µm boron doped p-type (100) Si wafer with resistivity of 3–-5 (WaferPro LLC) was covered with polyimide tape for protection before alternatively rinsing the surface with copious amounts of DI water and acetone, where water was used as the final rinse. The wafer was then immersed in 5% HF for 1– 2 min to remove the native SiO_2 layer. The wafer was then quickly rinsed with DI water and immersed in a 1 mM $AgNO_3$/1 wt% HF solution for 30 s to deposit the etching catalyst, followed by a quick DI water rinse, and then followed by 6 min in a "burial" solution consisting of 30% H_2O_2 and 3.2 wt% HF in a 1:100 volumetric ratio. During this step, nanochannels were formed under each silver cluster deposited on the surface as the metal is driven downwards through the material. This could be seen as the wafer transitions from shiny grey to matte black while evolving H_2. After this step, the wafer was rinsed with water and then cleaned in 35% HNO_3 for 6 min to remove the silver deposits on the bottom of the newly formed channels. The bSi was then rinsed one final time and dried with nitrogen. The large-channel c-bSi (c_{LP}-bSi) was synthesized from the same procedure, except the Ag deposition time was increased to 60 s.

Sinuous Nanoporous Black Silicon Fabrication: The same fabrication technique was used for s-bSi with slight modification. The burial solution contained IPA in addition to 30% H_2O_2 and 3.2% HF at a volumetric ratio of 5 mL:85 uL:100 mL. The added IPA led to high tortuosity in the structure.[23] The burial time also increased to 8 min to form channels which were similar in depth to c-bSi and achieved identical surface coverage.

Platinum Deposition: The as-prepared bSi was cleaned with N_2 to remove surface macroparticles, then further cleaned in 5% HF for 30 s

to remove surface oxides. After a quick DI water rinse, the sample was submerged in 5 mM K_2PtCl_5/1% HF for 60 s. The sample was then quickly rinsed with DI water and dried under N_2.

Electron Microscopy Characterization: Both samples were characterized using a FEI Quanta 450 SEM operated at 25 kV equipped with an Oxford Aztec EDX detector. Samples were imaged on the top surface and cross section, where the latter sample was prepared by etching a piece of wafer partially across the nanostructured side with a diamond cutter then snapping the wafer such that the top surfaces do not touch in the process. The sample was then mounted on a vertical platform for SEM and imaged on the unetched portion of the exposed edge.

Scanning Transmission Electron Microscopy Sample Preparation: Electron transparent TEM thin foils were prepared using a FEI Helios Dual Beam focus ion beam (FIB) instrument. The samples were first coated with a C layer to minimize sample drift inside the FIB and improve sample conductivity. Within the FIB, fine-to-coarse grained gradient ion beam platinum layers were deposited over a 15 µm by 3 µm area with a thickness of 3 µm. A thin foil lift out preceded over this rectangular area with final lamellae measured as 13 µm by 5 µm with a nominal initial thickness of 0.7 µm. Subsequently, the lamellae was mounted using a molybdenum Omni probe TEM grid and thinned using a 5 kV gallium beam to less than 110 nm in total thickness for examination. Final cleaning was performed using a 1 kV gallium beam to reduce additional curtaining and milling damage.

Electron Microscopy Characterization: The nanoporous Si sample morphologies were characterized using an FEI Quanta 450 FEG microscope at 20 kV with a spot size of 3.0. A JEOL 2800 high throughput TEM equipped with dual high solid angle 30 mm^2 windowless Si X-ray detectors was operated in high resolution TEM and STEM modes at 200 kV. For STEM analysis, a nanometer-sized probe, with a total beam current of less than 110 pA, was used for sample analysis. The inelastically scattered electrons passing through the electron transparent sample were used to collect a high angle annular dark field (HAADF) image. Energy dispersive X-ray spectroscopy (EDX) was operated under the same conditions to acquire the Si-K, Ti-K/L, O-K, and Pt-L with the best achievable spatial and energy resolution. Multiple 10 s scans over 256 × 256 pixels were performed to acquire quantitative measurements over single acquisition. Cliff–Lorimer thin film correction and Thermo Scientific software were used to process EDX spectra and calculate the weighted atomic percent spectral maps. Matlab was used to visualize the weighted spectral images. These nominalized maps were compared against the accompanying HAADF image, allowing for quantitative determination of differences in sample thickness resulting from particles, tracks, and pores.

Photoelectrode Fabrication: Photoelectrodes were made using a previously reported method with minor modifications.[23] Briefly, the electrode bases were prepared in advance by coiling 18 gauge copper wire into a planar spiral of ≈1 cm radius with a 10 cm straight tail, which was placed inside a narrow glass tube ≈2 inches long. A small amount of excess wire was left coming out of the tube for attachment to instruments. Next, the wafers were prepared. First, the polyimide tape was removed from the back before cutting the wafer into ≈0.2 cm^2 pieces. Each piece was placed in 5% HF for 30 s to remove the native oxide layer before forming the Ohmic contact. A Ga-In eutectic alloy was applied to the back of the wafer, and conductive silver paint was applied to the copper spiral. The wafer was placed Ga-In side down onto the spiral and allowed to dry. During this time, the first layer of epoxy (Loctite 9462 Hysol) was prepared to isolate the copper from solution during testing. The epoxy was applied to the back, sides, and face of the copper spiral until the edges of the wafer were covered and the gap between the spiral and the glass was sealed. The electrode was then allowed to dry for 24 h. A second layer of epoxy (Loctite E-120 HP) was applied to protect the first sealant layer from damage in acidic or basic solution. This layer was also allowed 24 h to dry before use.

Photoelectrochemical Measurements: All PEC measurements were made using a 300 W Xe-arc lamp with a water filter for IR light filtration and a CHI 660E electrochemical workstation unless otherwise specified. The light intensity was calibrated to 1 sun (100 mW cm^{-2}) using a thermal sensor (Thorlabs) prior to and following each measurement. LSV was used to determine the onset and saturation potentials of each electrode, where a platinum wire served as the counter electrode and Ag/AgCl (saturated) as the reference electrode. The measured potential was converted to RHE using E(RHE) = E(Ag/AgCl) + 0.197 V + 0.059 pH. IPCE was measured using the same light source and workstation, where the water filter was replaced with the ≈10 nm bandpass filter. Each wavelength was tested for 100 s while chopping the light in 10 s intervals. Long-term electrolysis and IPCE were performed at the saturation potentials, and impedance testing was performed at the onset potentials. IPCE was calculated using the equation below,

$$\mathrm{IPCE} = \frac{1243 \times I \times S_1}{\lambda \times P \times S_2} \tag{4}$$

where I was the current (mA), S_1 was the light detector surface area (cm^2), S_2 was sample surface area (cm^2), λ was the wavelength (nm), and P was the light power (mW).

Tafel slopes were calculated using a program developed by Agbo et al. which recursively minimizes the residue of the current density/overpotential differential for the inputted LSV, thereby obtaining the optimized potential width for Tafel fitting (Figures S12 and S13, Supporting Information).[34] These values were confirmed by manual calculation of the slopes in the optimized potential ranges. Standard Tafel analysis was also performed to confirm the program-predicted values. Manual Tafel analysis was performed by converting raw LSV data to current density (J, mA cm^{-2}) and potential in mV versus RHE. A Tafel plot was produced by plotting log|J| on the independent axis and potential on the dependent axis. Linear fitting was performed in the center region of the Tafel plot, corresponding to the onset range in the LSV (Figure S14, Supporting Information). The manually calculated slopes corresponded well with results from the optimization program developed by Agbo et al.; however, different slopes were obtained depending on the manually fitted region.

Supporting Information

Supporting Information is available from the Wiley Online Library or from the author.

Acknowledgements

M.P. and F.Y. contributed equally to this work. The authors want to acknowledge SDSU startup funds and the SDSU University Grants Program for their support in this research. J.A.A. was partially supported by the INL Laboratory Directed Research & Development (LDRD) Program under DOE Idaho Operations Office Contract DE-AC07-05ID14517.

Conflict of Interest

The authors declare no conflict of interest.

Data Availability Statement

The data that supports the findings of this study are available in the supplementary material of this article.

Keywords

black silicon, hydrogen evolution reaction, photoelectrochemical conversion, solar energy conversion, structure-induced stability

Received: October 18, 2020
Revised: January 25, 2021
Published online: February 18, 2021

[1] J. Barber, *Chem. Soc. Rev.* **2009**, *38*, 185.
[2] N. S. Lewis, D. G. Nocera, *Proc. Natl. Acad. Sci. USA* **2007**, *104*, 20142.
[3] M. Ali, F. Zhou, K. Chen, C. Kotzur, C. Xiao, L. Bourgeois, X. Zhang, D. R. MacFarlane, *Nat. Commun.* **2016**, *7*, 11335.
[4] S. Wang, X. Hai, X. Ding, K. Chang, Y. Xiang, X. Meng, Z. Yang, H. Chen, J. Ye, *Adv. Mater.* **2017**, *29*, 1701774.
[5] S. Licht, *Adv. Mater.* **2011**, *23*, 5592.
[6] K. Sivula, R. van de Krol, *Nat. Rev. Mater.* **2016**, *1*, 15010.
[7] Y. Zhao, N. C. Anderson, M. W. Ratzloff, D. W. Mulder, K. Zhu, J. A. Turner, N. R. Neale, P. W. King, H. M. Branz, *ACS Appl. Mater. Interfaces* **2016**, *8*, 14481.
[8] R. Sathre, C. D. Scown, W. R. Morrow, J. C. Stevens, I. D. Sharp, J. W. Ager, K. Walczak, F. A. Houle, J. B. Greenblatt, *Energy Environ. Sci.* **2014**, *7*, 3264.
[9] J. L. Young, M. A. Steiner, H. Döscher, R. M. France, J. A. Turner, T. G. Deutsch, *Nat. Energy* **2017**, *2*, 17028.
[10] S. Hu, C. Xiang, S. Haussener, A. D. Berger, N. S. Lewis, *Energy Environ. Sci.* **2013**, *6*, 2984.
[11] A. Kudo, Y. Miseki, *Chem. Soc. Rev.* **2009**, *38*, 253.
[12] J. Oh, T. G. Deutsch, H. C. Yuan, H. M. Branz, *Energy Environ. Sci.* **2011**, *4*, 1690.
[13] H. Zhong, A. Guo, G. Guo, W. Li, Y. Jiang, *Nanoscale Res. Lett.* **2016**, *11*, 322.
[14] Q. Tan, F. Lu, C. Xue, W. Zhang, L. Lin, J. Xiong, *Sens. Actuators, A* **2019**, *295*, 560.
[15] J. Lv, T. Zhang, P. Zhang, Y. Zhao, S. Li, *Nanoscale Res. Lett.* **2018**, *13*, 110.
[16] X. Liu, P. R. Coxon, M. Peters, B. Hoex, J. M. Cole, D. J. Fray, *Energy Environ. Sci.* **2014**, *7*, 3223.
[17] F. Toor, J. B. Miller, L. M. Davidson, L. Nichols, W. Duan, M. P. Jura, J. Yim, J. Forziati, M. R. Black, *Nanotechnology* **2016**, *27*, 412003.
[18] W. C. Wang, M. C. Tsai, J. Yang, C. Hsu, M. J. Chen, *ACS Appl. Mater. Interfaces* **2015**, *7*, 10228.
[19] M. J. Choi, J. Y. Jung, M. J. Park, J. W. Song, J. H. Lee, J. H. Bang, *J. Mater. Chem. A* **2014**, *2*, 2928.
[20] Z. Kang, H. Si, S. Zhang, J. Wu, Y. Sun, Q. Liao, Z. Zhang, Y. Zhang, *Adv. Funct. Mater.* **2019**, *29*, 1808032.
[21] S. Cao, Z. Kang, Y. Yu, J. Du, L. German, J. Li, X. Yan, X. Wang, Y. Zhang, *Adv. Energy Mater.* **2020**, *10*, 1902985.
[22] F. Yang, J. A. Aguiar, M. Fairchild, W. Vakki, S. Younan, Y. Zhou, L. Zhuo, J. Gu, *Adv. Mater. Interfaces* **2019**, *6*, 1802085.
[23] L. Lu, W. Vakki, J. A. Aguiar, C. Xiao, K. Hurst, M. Fairchild, X. Chen, F. Yang, J. Gu, Z. J. Ren, *Energy Environ. Sci.* **2019**, *12*, 1088.
[24] E. Abdur-Rahman, I. Alghoraibi, H. Alkurdi, *Int. J. Anal. Chem.* **2017**, *2017*, 7542870.
[25] M. Ju, N. Balaji, C. Park, H. T. T. Nguyen, J. Cui, D. Oh, M. Jeon, J. Kang, G. Shim, J. Yi, *RSC Adv.* **2016**, *6*, 49831.
[26] J. Kegel, H. Angermann, U. Stürzebecher, B. Stegemann, *Energy Procedia* **2013**, *38*, 833.
[27] L. Romano, J. Vila-Comamala, K. Jefimovs, M. Stampanoni, *Microelectron. Eng.* **2017**, *177*, 59.
[28] Z. W. She, J. Kibsgaard, C. F. Dickens, I. Chorkendorff, J. K. Nørskov, T. F. Jaramillo, *Science* **2017**, *355*, eaad4998.
[29] W. Sheng, H. A. Gasteiger, Y. Shao-Horn, *J. Electrochem. Soc.* **2010**, *157*, B1529.
[30] L. Tsybeskov, K. L. Moore, D. G. Hall, P. M. Fauchet, *Phys. Rev. B* **1996**, *54*, R8361.
[31] L. He, C. Jiang, H. Wang, D. Lai, Rusli, *ACS Appl. Mater. Interfaces* **2012**, *4*, 1704.
[32] S. Fletcher, *J. Solid State Electrochem.* **2009**, *13*, 537.
[33] T. Shinagawa, A. T. Garcia-Esparza, K. Takanabe, *Sci. Rep.* **2015**, *5*, 13801.
[34] P. Agbo, N. Danilovic, *J. Phys. Chem. C* **2019**, *123*, 30252.
[35] T. H. Distefano, D. E. Eastman, *Solid State Commun.* **1971**, *9*, 2259.
[36] F. K. Crundwell, *ACS Omega* **2017**, *2*, 1116.
[37] M. Velazquez-Rizo, D. Iida, K. Ohkawa, *Sci. Rep.* **2020**, *10*, 12586.